LA-UR-21-22234
Accepted Manuscript

Crystal mechanics-based thermo-elastic constitutive modeling of orthorhombic uranium using generalized spherical harmonics and first-order bounding theories

Marki, Russell Eli
Brindley, Kyle Andrew
Mccabe, Rodney James
Knezevic, Marko

Provided by the author(s) and the Los Alamos National Laboratory (2023-08-24).

To be published in: Journal of Nuclear Materials

DOI to publisher's version: 10.1016/j.jnucmat.2021.153472

Permalink to record:
https://permalink.lanl.gov/object/view?what=info:lanl-repo/lareport/LA-UR-21-22234

Los Alamos NATIONAL LABORATORY

National Nuclear Security Administration

Los Alamos National Laboratory, an affirmative action/equal opportunity employer, is operated by Triad National Security, LLC for the National Nuclear Security Administration of U.S. Department of Energy under contract 89233218CNA000001. By approving this article, the publisher recognizes that the U.S. Government retains nonexclusive, royalty-free license to publish or reproduce the published form of this contribution, or to allow others to do so, for U.S. Government purposes. Los Alamos National Laboratory requests that the publisher identify this article as work performed under the auspices of the U.S. Department of Energy. Los Alamos National Laboratory strongly supports academic freedom and a researcher's right to publish; as an institution, however, the Laboratory does not endorse the viewpoint of a publication or guarantee its technical correctness.

Crystal mechanics-based thermo-elastic constitutive modeling of orthorhombic uranium using generalized spherical harmonics and first-order bounding theories

Russell E. Marki [a], Kyle A. Brindley [b], Rodney J. McCabe [c], and Marko Knezevic [a,*]

[a] Department of Mechanical Engineering, University of New Hampshire, Durham, NH 03824, USA.

[b] Weapon Systems Division, Los Alamos National Laboratory, Los Alamos, NM, 87544, USA. [c] Materials Science and Technology Division, Los Alamos National Laboratory, Los Alamos, NM, 87545, USA.

Abstract

In earlier works, a mathematical procedure for invertible microstructure-property linkages was developed using computationally efficient spectral methods for polycrystalline cubic and hexagonal metals. This paper formulates such invertible microstructure–property linkages for orthorhombic polycrystalline metals relying on the generalized spherical harmonics (GSH) spectral basis. The procedure is used to compute property closures of orthorhombic polycrystals. The closures represent the complete set of theoretically possible combinations of effective properties for a selected material. The procedure relies on the first-order bounding theories and considers orientation distribution functions (ODFs) as the main microstructural descriptor influencing homogenized properties. Numerous examples of these closures involving second-rank thermal expansion and fourth-rank elastic stiffness tensorial properties over a broad range of temperatures are presented for α-uranium (α-U). In doing so, certain key properties of these closures are exploited to facilitate their computation with drastically reduced computational effort. Along with the recently developed GSH-based interpolation procedure for ODFs from coarsely spaced experimental measurement grids to finely spaced finite element mesh resolution grids [1], the developed computationally efficient ODF-effective property linkages are used to establish a crystal mechanics-based simulation framework coupled with the finite element method (FEM). The ODF dependent thermal expansion and elastic stiffness tensors are efficiently calculated at every integration point and used by the FEM to predict the overall distortion of a hemispherical part made of α-U during heating. It is shown that the developed framework can be used to simulate microstructurally heterogeneous components under thermo-mechanical loadings in a computationally efficient manner.

* Corresponding author at:
marko.knezevic@unh.edu (M. Knezevic).

1. Introduction

Mathematical frameworks are being developed to treat microstructure as a variable in engineering design and optimization of components [2-5]. Essential for such frameworks is formulating invertible, i.e. bi-directional, linkages between microstructure and material properties with such linkages aimed at the identification of microstructures that are theoretically predicted to exhibit a desired combination of properties/performances [3, 6]. The spectral representation of material properties and microstructure has been shown to be an effective approach to establish invertible linkages. The approach involves constructing a space of all theoretically possible microstructures. Specifically, the space that includes all possible orientation distribution functions (ODFs) is referred to as the texture hull [3, 6-9]. Generalized spherical harmonics (GSH) have been shown to facilitate the most compact spectral representations of ODF dependent material properties, which is attributed to their ability to reflect the crystal and sample symmetries [10-12]. Calculating material properties corresponding to the texture hull using ODF-property linkages defines another space, which is the space of all theoretically possible properties for a given material. This space was originally referred to as the G-closures [13-16] and later as the property closures [17].

A number of property closures have been presented in the literature for both cubic and hexagonal metals including elastic [8, 17-19], plastic [20], and functional properties such as piezoelectric [21]. These closures were based on first-order bounding theories [22-26]. The procedure to delineate the property closures begins with building a database of non-zero GSH expansion coefficients for selected properties using integration over the orientation space. Next, expansion coefficients corresponding to the complete set of ODFs (the texture hull) are obtained. Finally, the expansion coefficients corresponding to the hull and the selected properties are linked to obtain the property bounds. Importantly, the spectral representations facilitate these calculations with dramatic reduction in computational time relative to traditional methods. The rapid evaluation using databases and spectral linkages is especially useful for accelerating the calculations of stress, strain hardening, and texture evolution pertaining to crystal plasticity models because iterative solution procedures such as those based on Newton's methods can be circumvented [20, 27, 28]. Having the bounds for a selected property combination, an optimization procedure is used to find ODFs corresponding to the boundary points in the property space [3, 17, 29, 30]. Invariant ODFs corresponding to the boundary points of the closures for a class of metals facilitate rapid delineation of property closures for that class of metals [18].

The two essential constructs, the closures and hulls, have been used in the theoretical microstructure sensitive design of components to improve their performances. Microstructures and associated properties have been identified to maximize compliant beam deflection [3], flywheel energy storage [31], the load bearing capacity of a thin plate with a central hole [6], and the minimized driving force of a crack in rotating disks [32] and thin-walled vessels [33]. In these studies, the ODF was the microstructural feature governing the relevant properties. However, similar studies exist for designing compositional variations of fiber reinforced composites [34-36]. A design strategy referred to as topology optimization was developed specifically for designing composite materials for extreme mechanical and functional properties [37-40].

This paper conceives a computationally efficient procedure for the invertible microstructure–property linkages homogenizing second-rank and fourth-rank tensorial properties for

orthorhombic polycrystalline metals. The development of this new procedure using the GSH basis will be described. The procedure is used to compute property closures of orthorhombic polycrystals. Numerous examples of thermal expansion and elastic property closures covering a broad range of temperatures are computed and presented for α-uranium (α-U). Furthermore, the procedure is coupled with the finite element method (FEM) to model anisotropic thermo-elastic material response of polycrystalline orthorhombic metal components. For such modeling, the spatially resolved distributions of microstructural features is considered over the finely discretized component geometry, i.e. FE mesh. Considering that experimental characterization of spatial location-dependent microstructural data is limited to a finite number of locations, it is necessary to interpolate the data from coarsely spaced experimental grids to finely spaced finite element mesh grids. A robust interpolation scheme has recently been developed to interpolate ODFs. This scheme exploits the linearity of the GSH space in which the expansion coefficients representing ODFs are interpolated over a given variable such as space [1]. These recent advances addressing the interpolation of ODFs and the computationally efficient procedure for the ODF-property linkages described here are combined to calculate the spatial variation of the ODF-dependent thermal expansion and elastic stiffness. This novel crystal mechanics-based simulation methodology is used to predict the overall distortion of a hemispherical part made of α-U during heating using the FEM. The spatial variation of texture data is obtained by neutron diffraction measurements and subsequently interpolated to initialize the material points of the FE mesh. Hence, the simulation is carried out with the knowledge of texture and single crystal constants at each FE integration point. Anisotropic distortion is predicted. This distortion is due to the crystallographic texture and highly anisotropic elastic stiffness and thermal expansion coefficients of the low symmetry crystal structure of α-U. Results, computational efficiency, and insights of this microstructurally heterogeneous simulation are presented and discussed in this paper.

2. Representation of ODF using GSH and texture hull

An ODF, $f(g)$, is a statistical density function defining the volume fraction of crystal lattice orientations, g, in a polycrystalline material of volume, *V*. It is mathematically expressed as

$$f(g)dg = \frac{dV}{V}, \int_{OS} f(g)dg = 1. \quad (1)$$

In this work, the orientation, *g*, will be described using the set of three Bunge-Euler rotation angles (ϕ_1, Φ, ϕ_2). The Bunge-Euler orientation space (*OS*) is defined by these three rotation angles. In Eq. (1), dV is the increment in volume containing crystal lattice orientations within the increment, dg, in the *OS* [10, 41]. Although $f(g)$ can be expressed in its discrete form [42], the continuous form is required for its GSH representation. The development of spectral representations of the ODF and material properties using GSH has been most successful for the

Bunge-Euler *OS* [4], in comparison with other orientation spaces: Rodriguez vectors [43], angle-axis pairs [44], or quaternions [45]. The ODF in a GSH series is

$$f(g) = \sum_{l=0}^{\infty} \sum_{\mu=1}^{M(l)} \sum_{n=1}^{N(l)} F_l^{\mu n} \dot{T}_l^{\mu n}(g), \tag{2}$$

where $\dot{T}_l^{\mu n}(g)$ is the orthorhombic-triclinic GSH function of relevance to the present work and $F_l^{\mu n}$ are the expansion coefficients. The Bunge-Euler angles are contained within the function, $\dot{T}_l^{\mu n}(g)$ [10]. The number of (l, μ, n) combinations depends on the symmetry (orthorhombic-triclinic) and the chosen rank for l (L). The chosen rank is labeled by "L", while "l" continuously enumerates the indices from 0 to L. Each triplet is one expansion coefficient; and the number of expansion coefficients is the number of dimensions in the expansion space.

The orthogonality relationship for the GSH functions is used in evaluating the expansion coefficients as

$$\int_{OS} \dot{T}_l^{\mu n}(g)\, \dot{T}_{l'}^{*\mu' n'}(g)\, dg = \frac{1}{2l+1} \delta_{ll'} \delta_{\mu\mu'} \delta_{nn'}, \tag{3a}$$

$$\int_{OS} f(g)\, \dot{T}_l^{*\mu n}(g)\, dg = \sum_{l'=0}^{\infty} \sum_{\mu'=1}^{M(l')} \sum_{n'=1}^{N(l')} F_{l'}^{\mu' n'} \int_{OS} \dot{T}_{l'}^{\mu' n'}(g)\, \dot{T}_l^{*\mu n}(g)\, dg, \tag{3b}$$

$$\bar{F}_l^{\mu n} = (2l+1) \int_{OS} f(g) \dot{T}_l^{*\mu n}(g)\, dg. \tag{3c}$$

The symbol (*) asterisk in the superscript indicates the complex conjugate, while the invariant $dg = \sin(\Phi)\, d\phi_1 d\Phi\, d\phi_2$. The lower case delta, δ_{ij}, is Kronecker's delta. The expansion coefficients corresponding to an individual crystal orientation, g_k, are

$${}^k F_l^{\mu n} = (2l+1) \dot{T}^{*\mu n}_l(g_k). \tag{4}$$

A given ODF is usually described by a number of discrete orientations, N_{crys}, which are weighted by their volume fraction, α. In this case, Eq. (3c) is equivalent to

$$\bar{F}_l^{\mu n} = \sum_{k=1}^{N_{crys}} {}^k\alpha\, {}^k F_l^{\mu n}, \sum_{k=1}^{N_{crys}} {}^k\alpha = 1, 0 < {}^k\alpha < 1. \tag{5}$$

The bar is placed on top of F to indicate the volume average. The linearity of the expansion space allows the weighted expression.

The coefficients with the coordinates ${}^k F_l^{\mu n}$ for an orientation k can be plotted as a point in the expansion space. Creating such plot of points for many orientations, N_{crys}, makes up a texture hull, $M^k = \left\{ {}^k F_l^{\mu n} \mid {}^k F_l^{\mu n} = (2l+1) \dot{T}_l^{*\mu n}(g^k), g^k \in OS \right\}$. The hull is a convex and compact space because any empty space can be filled up with points of weighted combinations, $M = \left\{ \bar{F}_l^{\mu n} \mid \bar{F}_l^{\mu n} = \sum_k {}^k\alpha\, {}^k F_l^{\mu n}, {}^k F_l^{\mu n} \in M^k, {}^k\alpha \geq 0, \sum_k {}^k\alpha = 1 \right\}$. As a result, the hull, M, represents the complete set of all physically possible ODFs. While the hull can be represented to

infinity, the number of relevant dimensions depends on a selected ODF-property relationship represented in a GSH series. As will be described shortly, the representation of the ODF-elastic stiffness tensor relationship requires only $L = 4$ [18, 31]. The thermal expansion tensor requires only $L = 2$. Fig. 1 shows texture hulls for cubic and orthorhombic crystal structures with no sample symmetry i.e. triclinic sample symmetry. In the next sections, we describe the invertible ODF-property linkages for mapping the hulls in the material property space to delineate property closures. The closures represent the complete set of theoretically possible combinations of effective properties for a selected material.

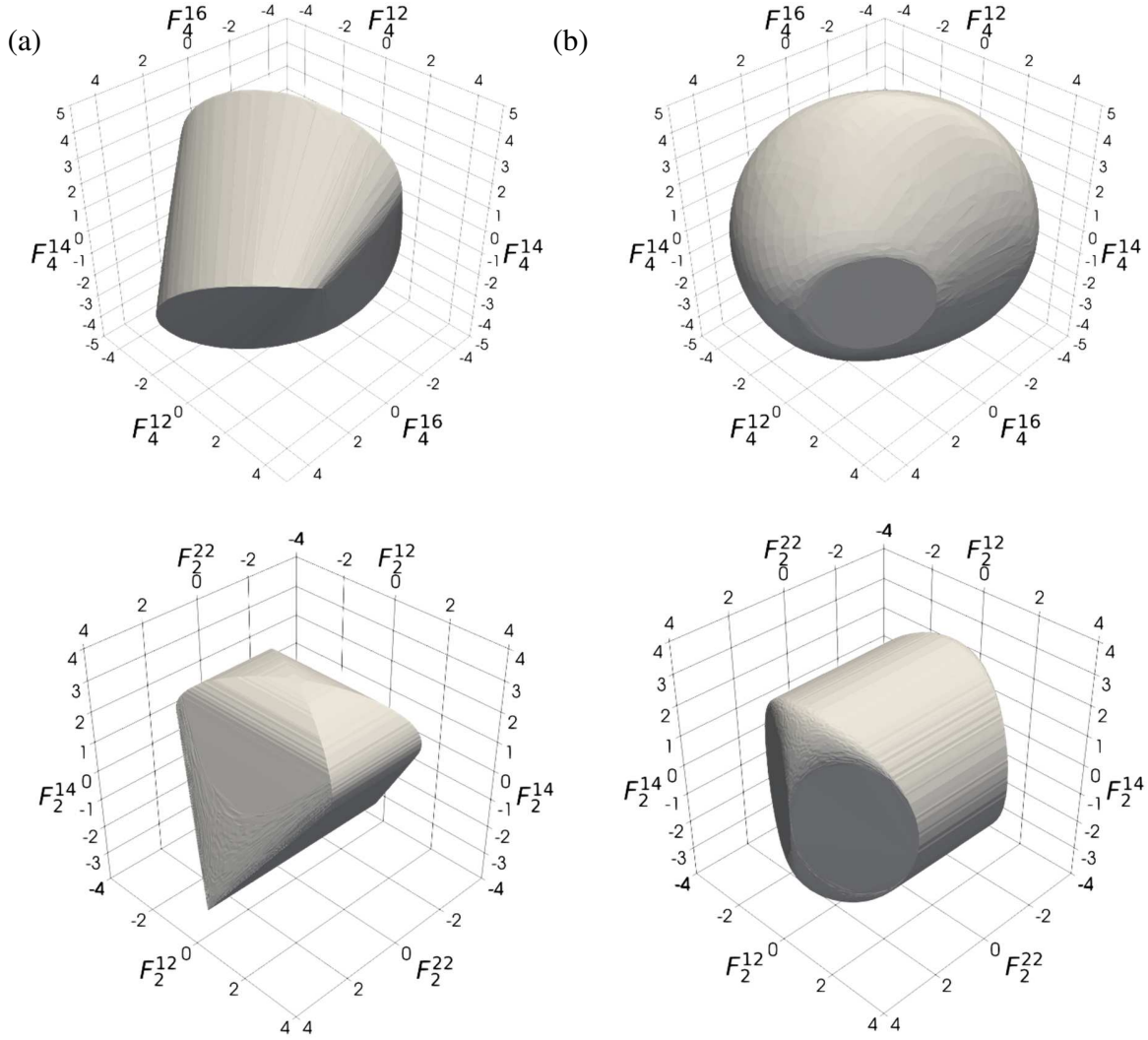

Figure 1. Examples of the GSH-based texture hulls for cubic-triclinic (top row) and orthorhombic-triclinic (bottom row) metals: (a) real and (b) imaginary arbitrarily selected

projections of F_4^{12}, F_4^{14}, and F_4^{16} for cubic-triclinic and F_2^{12}, F_2^{14}, and F_2^{22} for orthorhombic-triclinic are shown.

3. Representation of thermo-elastic properties using GSH

In a first-order approach, the coupled thermo-elastic constitutive behavior of relevance to the present work is described by adding the strains produced by stress and temperature fields. The thermo-elastic stress-strain relationship is expressed as

$$\boldsymbol{\varepsilon} = \boldsymbol{\varepsilon}^{el} + \boldsymbol{\varepsilon}^{th} = \bar{\mathbf{S}}^{s}\boldsymbol{\sigma} + \bar{\boldsymbol{\alpha}}^{s}\Delta T\,, \tag{6}$$

where the first term is the elastic (mechanical) strain and the second term is the strain induced by the thermal field. We will use bold letters to denote tensors, while italic and non-bold letters denote tensor components. $\bar{\mathbf{S}}^{s}$ is a symmetric 4th-rank elastic compliance tensor describing the elastic material behavior, $\bar{\boldsymbol{\alpha}}^{s}$ is a symmetric 2nd-rank tensor describing the thermal expansion of the material, $\boldsymbol{\sigma}$ is the Cauchy stress, and ΔT is the change in temperature from a chosen reference.

The elastic and thermal expansion tensors in the sample frame, *s*, depend on the crystal orientation and the fundamental crystal constants embedded in the $\mathbf{S}^{c}$, $\mathbf{C}^{c}$ ($\mathbf{C}^{c} = \left(\mathbf{S}^{c}\right)^{-1}$), and $\boldsymbol{\alpha}^{c}$ tensors in the crystal frame, *c*. $\mathbf{C}^{c}$ is a symmetric 4th-rank elastic stiffness tensor in the crystal frame. Fig. 2 shows the elastic [46] and thermal expansion [47] single crystal coefficients for α-U as a function of temperature. The components of the tensors in the sample frame can be obtained from those in the crystal frame using

$$C^{s}_{ijkl} = Q_{ip}Q_{jq}Q_{kr}Q_{ls}\,C^{c}_{pqrs}\,, \tag{7}$$

$$S^{s}_{ijkl} = Q_{ip}Q_{jq}Q_{kr}Q_{ls}\,S^{c}_{pqrs}\,, \tag{8}$$

$$\alpha^{s}_{ij} = Q_{ip}Q_{jq}\alpha^{c}_{pq}\,. \tag{9}$$

As an example, the equivalent expression in the component form for the elastic stiffness is $C^{s}_{ijkl} = Q_{ip}Q_{jq}Q_{kr}Q_{ls}\,C^{c}_{pqrs} = T_{ijklpqrs}C^{c}_{pqrs}$ with $\mathbf{Q}$ performing the coordinate transformation from the crystal frame, $\mathbf{e}^{c}_{i}$, to the sample frame, $\mathbf{e}^{s}_{i}$, using Bunge-Euler angles $g = (\phi_2, \Phi, \phi_2)$ as

$$\mathbf{Q} = \begin{bmatrix} \cos\phi_1\cos\phi_2 - \sin\phi_1\cos\Phi\sin\phi_2 & -\cos\phi_1\sin\phi_2 - \sin\phi_1\cos\Phi\sin\phi_2 & \sin\phi_1\sin\Phi \\ \sin\phi_1\cos\phi_2 + \cos\phi_1\cos\Phi\sin\phi_2 & -\sin\phi_1\sin\phi_2 + \cos\phi_1\cos\Phi\cos\phi_2 & -\cos\phi_1\sin\Phi \\ \sin\Phi\sin\phi_2 & \sin\Phi\cos\phi_2 & \cos\Phi \end{bmatrix} \tag{10}$$

Evaluating every component of the stiffness tensor involves 81 summations of the products, e.g. $C^{s}_{1111} = Q_{1p}Q_{1q}Q_{1r}Q_{1s}\,C^{c}_{pqrs}$. $T_{ijklpqrs}$ are the components of the orientation dependent transformation tensor, which when multiplied by C^{c}_{pqrs}, gives the components of C^{s}_{ijkl}. The tensor in its most general form has $3^8 = 6561$ components. However, the elastic stiffness has only 21 unique components in its most general form [48]. Taking the advantage of it, the tensor $\mathbf{T}$ reduces to

21*3*3*3*3 = 1701 different components. However, some of these components are equivalent resulting in 441 unique components. Knowing these 441 components, the entire $\mathbf{T}$ tensor can be populated. The orientation dependent transformation tensor for thermal expansion has $3^4 = 81$ components in its most general form. Since the thermal expansion tensor has 6 unique components, the transformation tensor reduces to 6*3*3 = 54 components. After eliminating equivalent components, the tensor has 36 unique components.

The orientation dependent transformation tensors (e.g. $\mathbf{T}(g)$) can be represented in a GSH series as

$$\mathbf{T} = \sum_{l=0}^{\infty} \sum_{\mu=1}^{M(l)} \sum_{\nu=1}^{N(l)} \mathbf{E}_l^{\mu n} \dot{T}_l^{\mu n}(g). \tag{11}$$

The integration over the orientation space must be performed to evaluate the orientation invariant expansion coefficients for the components of the thermal expansion and elastic stiffness/compliance tensors. Specifically, the integration to evaluate the coefficients $\mathbf{E}_l^{\mu n}$ is performed analytically in Matlab given the values of $\mathbf{T}(g)$, which are obtained using Eqs. (7) – (9). The integration also takes advantage of the orthogonality relation, Eq. (3), as

$$\mathbf{E}_l^{\mu n} = (2l+1) \int_{OS} \mathbf{T}(g) \dot{T}_l^{*\mu n}(g)\, dg\,. \tag{12}$$

This representation is particularly useful because it includes a finite number of non-zero expansion coefficients. Without the first frequency ($Re = 1$, $Im = 0$), the number of complex-value expansion coefficients is 44 for the elastic properties and 10 for thermal expansion properties. These correspond to $L = 4$ and $L = 2$, respectively. The coefficients corresponding to ranks higher than these evaluate to zero. The result of the integration will be denoted by $\mathbf{E}_l^{\mu n}$. Although Eqs. (11) and (12) are specific to $T_{ijklpqrs}(g)$ used in the equations for stiffness and compliance tensors, an equivalent expressions exist for the orientation dependent transformation tensor, $Q_{ip}Q_{jq}$, for the thermal expansion. Since completely equivalent, it is not provided. The elastic property coefficients $\mathbf{E}_l^{\mu n}$ (441 components) and thermal expansion property coefficients (36 components) for the orientation dependent transformation tensor are the database, which can be recursively used to evaluate $\mathbf{C}^s$, $\mathbf{S}^s$, $\boldsymbol{\alpha}^s$, as will be elaborated shortly. Given the number of components and the number of expansion coefficients per component, the databases per tensor are regarded as compact.

We now turn our attention to calculating volume average properties. Average mechanical properties of polycrystals like $\bar{\mathbf{C}}^s$, $\bar{\mathbf{S}}^s$, and $\bar{\boldsymbol{\alpha}}^s$ tensors can be estimated from those of single crystals by homogenization with a weight function, i.e. the ODF, $f(g)$. For the 4th-rank elastic stiffness tensor, $\bar{\mathbf{C}}^s$, the formula is [49]

$$\bar{\mathbf{C}}^s = \frac{1}{V}\int_V \mathbf{C}^s(\mathbf{x})\,d\mathbf{x} = \bar{\mathbf{T}}\mathbf{C}^c = \int_{OS} \mathbf{T}(g)\, f(g)\, dg\, \mathbf{C}^c = \sum_{l=0}^{L=4}\sum_{\mu=1}^{M(l)}\sum_{n=1}^{N(l)} \frac{1}{2l+1}\mathbf{E}_l^{\mu n}\bar{F}_l^{\mu n}\,\mathbf{C}^c. \quad (13)$$

Calculation of a homogenized elastic stiffness (Eq. 13) requires the coefficients of the GSH expansion of the ODF function, $\bar{F}_l^{\mu n}$, up to fourth order ($L = 4$) coefficients for $\mathbf{T}(g)$, and the crystal tensor $\mathbf{C}^c$. The expression for $\bar{\mathbf{S}}^s$ in the same except $\mathbf{S}^c$ is used instead of $\mathbf{C}^c$. Equivalently, for the calculation of $\bar{\boldsymbol{\alpha}}^s$, the equation requires $\bar{F}_l^{\mu n}$, up to second order ($L = 2$) expansion coefficients for the orientation tensor, and $\boldsymbol{\alpha}^c$ crystal tensor. As is evident, the calculation only involves summation of 44 numbers for $\bar{\mathbf{C}}^s$ (and $\bar{\mathbf{S}}^s$) and 10 numbers for $\bar{\boldsymbol{\alpha}}^s$ after the multiplication. As a result, the property calculation in the spectral representation is essentially instantaneous. Note that Eq. (13) can be used to calculate the crystal property or the volume average property in the sample frame depending on whether $F_l^{\mu n}$ or $\bar{F}_l^{\mu n}$ is supplied. Importantly, the number of calculations (multiplications and summations) remains the same. We emphasize, the databases are compact and the calculations are extremely efficient.

Figs. 3 and 4 show orientation dependent $C_{1111}(g)$ elastic stiffness and $\alpha_{11}(g)$ thermal expansion components over the cubic-triclinic and orthorhombic-triclinic fundamental zones of orientation space calculated using Eqs. (7) and (13) for $C_{1111}(g)$ and Eq. (9) and (13) for $\alpha_{11}(g)$. The calculations are performed for Cu and α-U. The calculations for Cu are included for verification because a type of the ODF-elastic stiffness spectral representation was presented in an earlier work [18]. This earlier work considered a compact form of the elastic stiffness available for cubic metals [48] as opposed to the general form i.e. Eq. (7). Since the compact form does not exist for orthorhombic metals, the representations presented in this paper are done using the general form of Eqs. (7) – (9) for both cubic and orthorhombic metals. The compact or general forms works equally well for cubic metals. Since the subfigures (a) and (b) representing the GSH and Q computations are identical within both Figs. 3 and 4, the GSH representations of the ODF-property relationships developed in the present work are validated.

In closing this section, we present the property bounds relevant to the delineation of property closures and subsequent FEM simulations. The expressions are given for the elastic stiffness only. The first-order lower and upper bounds for the diagonal components of the effective elastic stiffness are [22-24, 50]:

$$(\bar{S}^{-1})_{ijij} \leq C^*_{ijij} \leq \bar{C}_{ijij}. \quad (14)$$

The bounds for the off-diagonal components are

$$\max(\bar{C}_{ijkl}, (\bar{S}^{-1})_{ijkl}) - \sqrt{\Delta_{ijij}\Delta_{klkl}} \leq C^*_{ijkl} \leq \min(\bar{C}_{ijkl}, (\bar{S}^{-1})_{ijkl}) + \sqrt{\Delta_{ijij}\Delta_{klkl}}, \quad (15a)$$

$$\Delta_{ijkl} = \bar{C}_{ijkl} - (\bar{S}^{-1})_{ijkl}. \quad (15b)$$

Only in these two equations, no implicit summation on repeated indices is used. Note that for $(\bar{S}^{-1})_{abab}$, an inverse is taken after the homogenization.

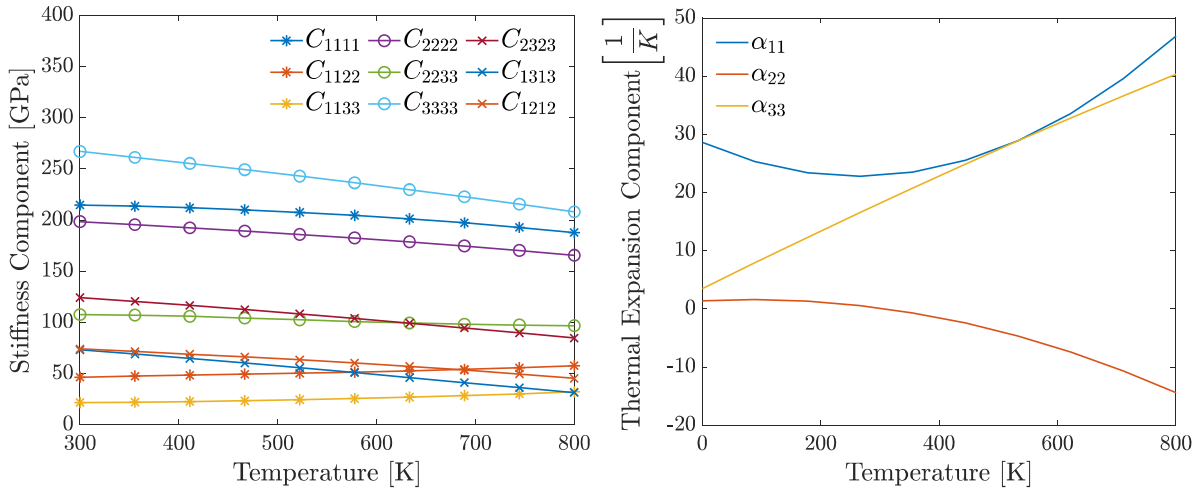

Figure 2. Elastic [46] and thermal expansion [47] single crystal coefficients for α-U as a function of temperature.

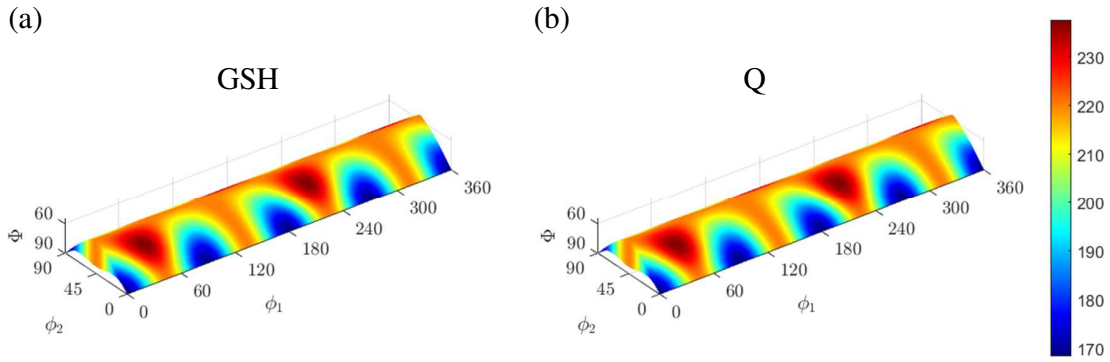

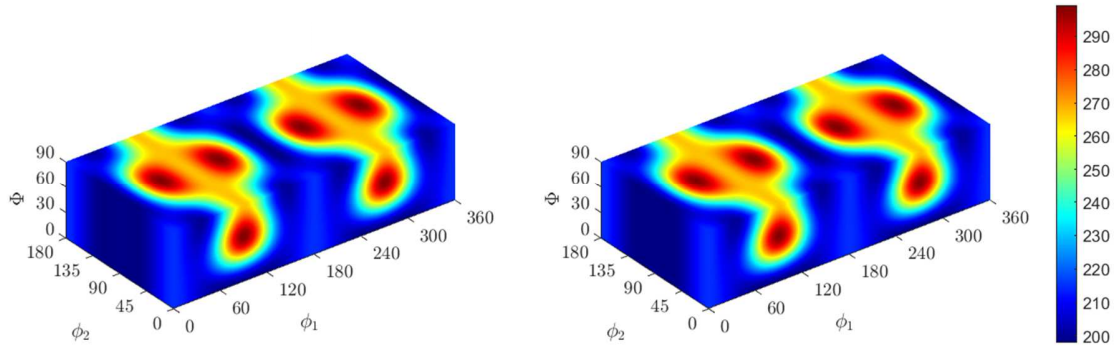

Figure 3. Contour plots of the C_{1111} elastic stiffness component in the cubic-triclinic (top row) and orthotropic-triclinic (bottom row) fundamental zones of the Bunge-Euler space for Cu and α-U, respectively: (a) computed using the GSH method (Eq. (13)) and (b) computed directly using Eq. (7) (Q method). The maximum difference between the two plots is of the order 10^{-13} GPa.

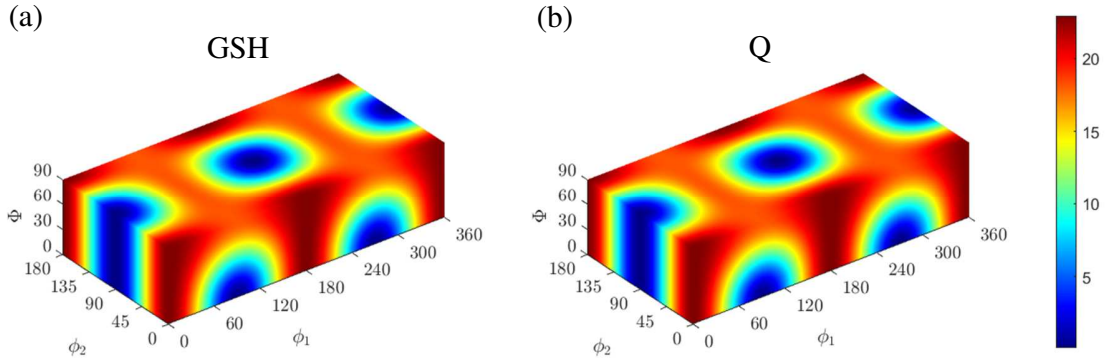

Figure 4. Contour plots of the α_{11} thermal expansion coefficient in the orthotropic-triclinic fundamental zone of the Bunge-Euler space for α-U (a) computed using the GSH method (an equivalent of Eq. (13)) and (b) computed directly using Eq. (9). The maximum difference between the two plots is of the order 10^{-13} K^{-1}.

4. Property closures

The spectral approach based on GSH has been used in prior works to delineate property closures for cubic and hexagonal metals [8, 17, 18]. These closures rely on the first-order bounding theories and consider ODFs as the main microstructural descriptors influencing the effective properties. In other works, these closures have been delineated using the spectral approaches based on fast Fourier transforms (FFTs) [42, 51]. The FFT approach facilitates delineating of closures more efficiently than the GSH approach. As an added advantage, the FFT computational methodology is more readily accessible than the GSH codes. However, the GSH

representation is more compact with fewer necessary expansion coefficients and resulting in smaller databases. This work advances the GSH approach for delineating property closures to orthorhombic polycrystals. To this end, the new ODF–property linkages formulated in the prior section are used to obtain the elastic stiffness and thermal expansion closures. The delineation procedure for closures relies on the database of non-zero GSH expansion coefficients for each component of the orientation dependent transformation tensors for calculating the thermal expansion and elastic stiffness/compliance tensors (e.g. $T_{ijklpqrs}$). Next, the expansion coefficients corresponding to a complete set of ODFs (the texture hull) must be calculated. Finally, the expansion coefficients corresponding to the ODFs and the properties are multiplied and summed and then multiplied with crystal properties to obtain the property bounds (i.e. Eq. 13). These calculations are performed with a dramatic reduction in computational time relative to traditional methods (i.e. Eqs. (7) - (9)).

The procedure starts with selecting a set of points in the texture hull "eigen textures" [52]. These eigen textures cover the fundamental region of the OS. The property bounds (Eqs. (14) and (15)) are then evaluated using the GSH representation of the ODF-to-property linkages (Eq. (13)) for all relevant properties ($\mathbf{C}^s$, $\mathbf{S}^s$, and $\boldsymbol{\alpha}^s$) for these eigen textures. Of these eigen textures, a set of those producing the boundary points of the property closure are selected for making combinations (pairs). These combinations are weighted textures corresponding to the boundary points of the closures. The weighted pairs are incremented by a 0.2 weighted fraction, i.e. from (0.2, 0.8) pair to (0.8, 0.2) pair. Calculating the relevant properties for these pairs ($\overline{\mathbf{C}}^s$, $\overline{\mathbf{S}}^s$, and $\overline{\boldsymbol{\alpha}}^s$) expands the property closures. Next, a new set of textures at the new boundary of the current closure are selected to evaluate properties ($\overline{\mathbf{C}}^s$, $\overline{\mathbf{S}}^s$, and $\overline{\boldsymbol{\alpha}}^s$) corresponding to their weighted combinations. This process is repeated until the expansion of closures is saturated. The procedure follows the ideas underlying genetic algorithms and was used in the past for cubic and hexagonal metals [20].

This procedure in conjunction with the novel GSH representation of properties, Eq. (13), is used here to obtain the first-order property closures for orthorhombic metals. However, before presenting results for orthorhombic metals, we verify the novel GSH representation of properties using cubic metals. For this purpose, we use polycrystalline Cu. As mentioned earlier, the compact form corresponding to Eqs. (7) and (8) has been used in the past for cubic and hexagonal metals. This is the first report using the most general expressions, Eqs. (7) – (9). The general expressions work for any crystal symmetry but are mandatory for orthorhombic symmetry as there is no a corresponding compact form. Fig. 5 presents the results for Cu. These results are identical to those presented in earlier works based on the GSH representation [18] and the FFTs representation [42] of the compact form elastic stiffness/compliance further verifying the spectral representation of the general expressions, Eqs. (7) – (9). The shaded region inside the closures denotes the possible property combinations for the stiffness components according to

the first-order bounding theories. Any property combination from the closures has corresponding textures inside the hull. Therefore, the ODF-property linkages are invertible.

Examples of elastic and thermal expansion property closures are presented for α-U in Figs. 6 and 7. These closures cover a broad range of temperatures because the crystal constants were available (Fig. 2). As with Cu, we present three examples of pairs of the effective properties. The particular property combination for the effective axial elastic component and the effective shear component play a role in the design of engineering parts experiencing a simultaneous axial load and twisting moment. Since the closures reported here are for triclinic textures, i.e. no sample symmetry assumed, it is possible to couple the additional normal-shear components. Note that when the orthotropic sample symmetry is invoked, $\bar{C}_{1112}$ is zero.

In delineating these closures for orthorhombic metals over the range of temperatures, certain key attributes are observed and exploited to facilitate their fast computation. Like for cubic metals [18], the expansion coefficients for orthorhombic metals corresponding to the boundary points on the closures are independent of the temperature dependent single crystal properties. Therefore, after computing and storing the set of ODF expansion coefficients corresponding to the boundary points on the closures at one temperature, this set of coefficients can be used to quickly produce closures at any other temperature. These ODF expansion coefficients are another database, which can be repeatedly used with single crystal properties at different temperature to rapidly delineate property closures at that temperature.

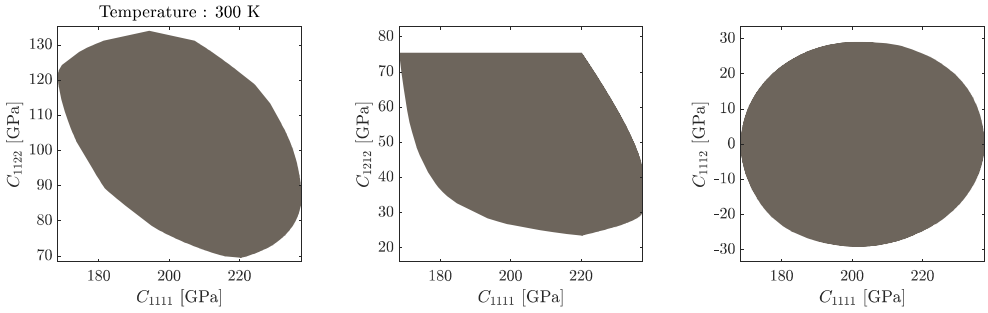

Figure 5. (C_{1111}, C_{1122}), (C_{1111}, C_{1212}), and (C_{1111}, C_{1112}) closures for Cu at room temperature computed using the GSH procedure presented in this paper.

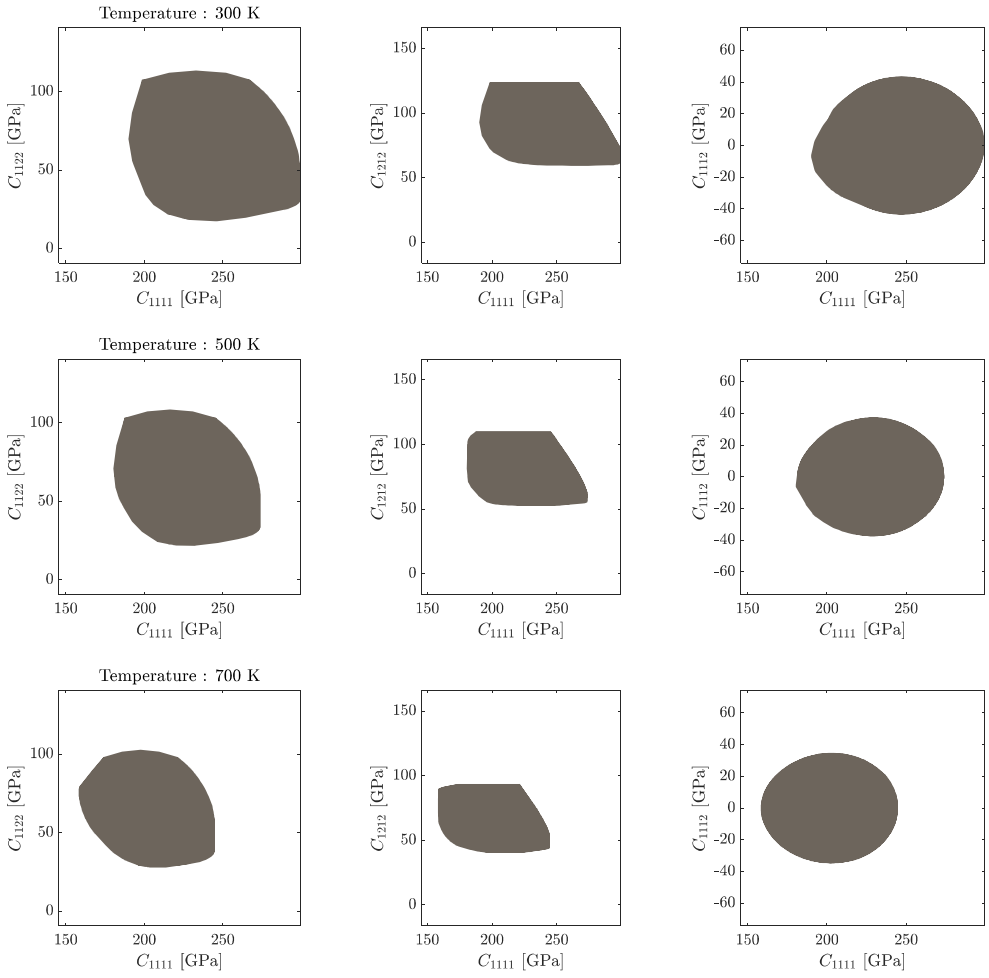

Figure 6. (C_{1111}, C_{1122}), (C_{1111}, C_{1212}), and (C_{1111}, C_{1112}) closures for α-U as a function of temperature computed using the GSH procedure presented in this paper.

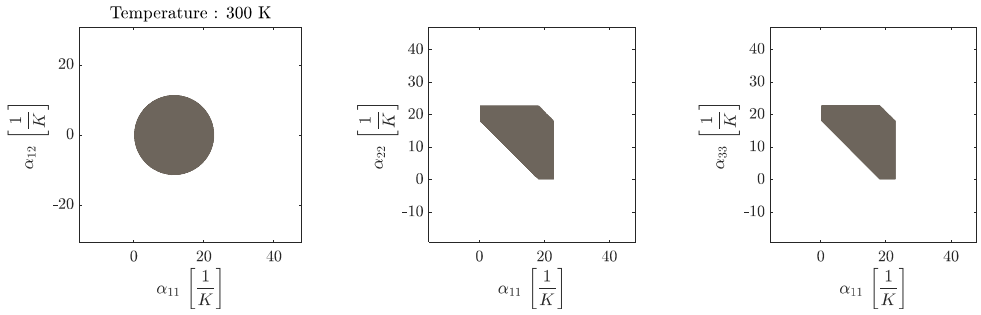

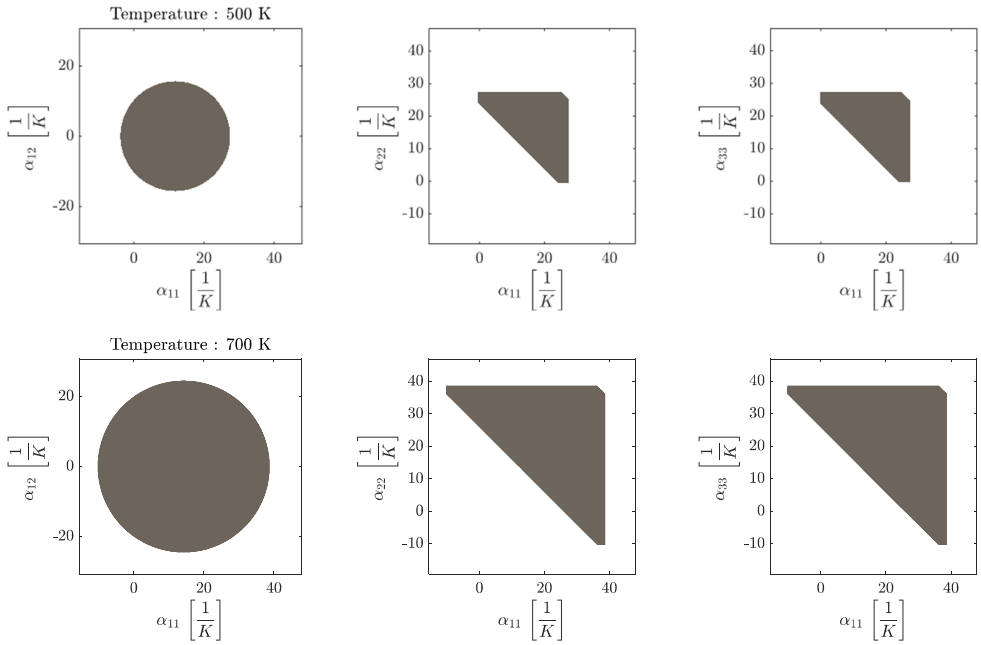

Figure 7. (α_{11}, α_{12}), (α_{11}, α_{22}) and (α_{11}, α_{33}) closures for α-U as a function of temperature computed using the GSH procedure presented in this paper.

5. Thermo-elastic simulation of hemispherical part during heating

In this section, we use the elastic stiffness and thermal expansion tensorial properties obtained based on the crystal mechanics at every integration point within finite elements in a thermo-elastic simulation. To this end, we develop a user material (UMAT) subroutine and combine it with a thermal expansion (UEXPAN) subroutine in Abaqus. A number of UMATs have been developed to embed texture and underlying anisotropy of material response at FE material points [53-55]. Of these UMATs, the implementation of the elasto-plastic self-consistent (FE-EPSC) polycrystal plasticity model is of interest in the present work [56, 57] because it is capable of predicting homogenized elasticity, thermal expansion, and plasticity [58]. Specifically, the UMAT we develop can calculate the elastic stiffness and thermal expansion tensorial properties either based on the GSH representation (Eq. 13) or the conventional calculations (Eqs. (7) – (9)) along with the underlying Jacobian matrix. The conventional calculations in the UMAT are used to verify the GSH calculations from the same UMAT. Moreover, the conventional calculations are used as a reference to demonstrate the computational efficiency of the GSH representation. Calculations using another UMAT, the FE-EPSC UMAT, are used to discuss the effect of the homogenization methodologies used in the prediction of the thermo-elastic distortion of the part (i.e. SC versus upper bound).

Fig. 8 shows the FE mesh of half of the hollow hemisphere. The hemisphere has an inner radius of 75 mm and an outer radius of 80 mm. Note, that the bottom has a small notch for fitting

in other parts. The mesh consists of 30,096 elements of which 528 are the coupled temperature-displacement triangular prism elements meeting at the pole cap (C3D6T) and the rest are full integration temperature-displacement elements (C3D8T) with 4 elements through the thickness. Nodal temperatures are prescribed to surface of the hemisphere starting at 25°C and increased to 250°C in increments of 1°C. The remaining imposed boundary conditions allow for free thermal expansion of the hemisphere since only two nodes are constrained (Fig. 8). One node has the encastre boundary condition, while the other is allowed only to move in the ND.

The novel crystal mechanics-based thermo-elastic constitutive modeling framework is aimed at modeling the spatial variation of anisotropic deformation during heating by accounting for the spatial variation of crystal lattice orientations of constituent grains and the temperature dependent single crystal properties across FE integration points. The first task is initialization of the spatial variation of texture by embedding the appropriate ODF at each FE integration point. Figs. 9 and 10 show pole figures of experimentally measured, neutron diffraction (NeD) texture data for a hemispherical part of depleted α-U. NeD is a bulk texture characterization technique over ~cm^3 volumes facilitated by the deep penetration of thermal neutrons into the material [59]. This measured data for half of the hemisphere is interpolated to the FE mesh resolution grid (Fig. 8). Assuming orthotropic sample symmetry, we rotate the data 180° around the ND two fold symmetry axis for each measured point to initialize the other half of the hemisphere. A rigorous procedure for the interpolation was presented in [1]. The procedure exploits the linearity of the GSH expansion space in the spatial interpolation/weighting of the expansion coefficients of measured ODFs. Upon interpolation, a corresponding ODF to the interpolated coefficients can readily be constructed by solving a linear programming problem in the expansion space [9, 60]. However, there is no need for reconstructing ODFs because the coefficients are sufficient for Eq. (13). Elegantly, the interpolated expansion coefficients are directly used in the ODF-property linkages (i.e. Eq. (13)). Nevertheless, the ODFs are reconstructed with the minimal number of 113 weighted orientations at each spatial location over the hemi to initialize the conventional simulation (Eqs. (7) – (9)) and the FE-EPSC simulation because these simulations require Bunge-Euler angles for texture at each FE integration point. 113 is the minimum number of weighted crystal orientations to facilitate a unique solution to an ODF given the expansion coefficients for orthorhombic-triclinic textures at $L = 10$. The heating simulations of the part can now be carried out taking into account the anisotropy because the thermo-elastic properties at each integration point are based on texture and temperature dependent single crystal constants.

Textures are interpolated to the centroid of each finite element of the hemisphere and assigned per element. Room temperature thermal expansion coefficients based on the interpolated textures at the centroids of each finite element are calculated and shown in Fig. 11. The coefficients of thermal expansion are calculated using the three material models (1) the upper bound GSH representation (denoted as GSH-UB), (2) the upper bound conventional calculations using the coordinate transformation matrix, $\mathbf{Q}$ (denoted as Q-UB), and (3) the self-consistent FE-EPSC (denoted as SC). As expected, GSH-UB and Q-UB results are identical. As is evident, the

thermal expansion contours reveal significant spatial variation in each thermal expansion tensor component over the hemispherical α-U part. Therefore, the distortion of the part predicted with the temperature change should be anisotropic.

Using the novel approach described here, the thermo-elastic heating simulation is performed using Abaqus implicit solver to study the geometric changes of a depleted α-U hemisphere. The simulation is carried out using the three material models (1) GSH-UB, (2) Q-UB, and (3) SC. Thermal strains are driven by the thermal expansion coefficients allowing Abaqus to define nodal displacements based on mechanical constraints. The simulation begins with a zero deformation step to initialize temperature, load interpolated textures at each integration point, and calculate the texture dependent thermal expansion coefficients and elastic constants within the UMAT. Next, the UEXPAN subroutine is called, given the change in temperature to estimate an increment in the thermal strain field ($\boldsymbol{\varepsilon}^{th} = \overline{\boldsymbol{\alpha}}^{s} \Delta T$) based on the thermal expansion coefficients (already calculated in the UMAT). Next, Abaqus estimates the mechanical strains ($\boldsymbol{\varepsilon}^{el} = \overline{\mathbf{S}}^{s} \boldsymbol{\sigma}$) given the boundary conditions. Finally, the UMAT subroutine is called to calculate stresses given the strains. The UMAT also recalculates the coefficients of thermal expansion and elastic stiffness for the next call to the UEXPAN subroutine.

Fig. 12 shows the predicted displacement fields and Fig. 13 shown the thermal strains plotted solely at the equator of the hemisphere after heating from 25°C and to 250°C. The fields indicate that the predicted distortion of the hemisphere with temperature is anisotropic. The predictions show location and directional dependence, which would not be possible to predict with isotropic models. The material also exhibits highly anisotropic plasticity behavior [61, 62]. In closing, Fig. 14 shows the computational time involved and memory requirements for the heating simulation as a function of the number of orientations embedded at each integration point for the GSH-UB and Q-UB computational methods. The purpose of these simulations was only to demonstrate the superiority of the GSH method. Simulations were performed on a workstation: Intel(R) Xeon(R) Gold 6130 CPU @ 2.10GHz with 32 cores and 772 GB RAM. 30 cores were used to carry out the heating simulations. The time involved and memory required in GSH-UB is constant, while these increase approximately linearly with the number of orientations for the Q-UB computational method. Results for SC are not shown. The SC simulation is the slowest by far because it requires the self-consistent iterations.

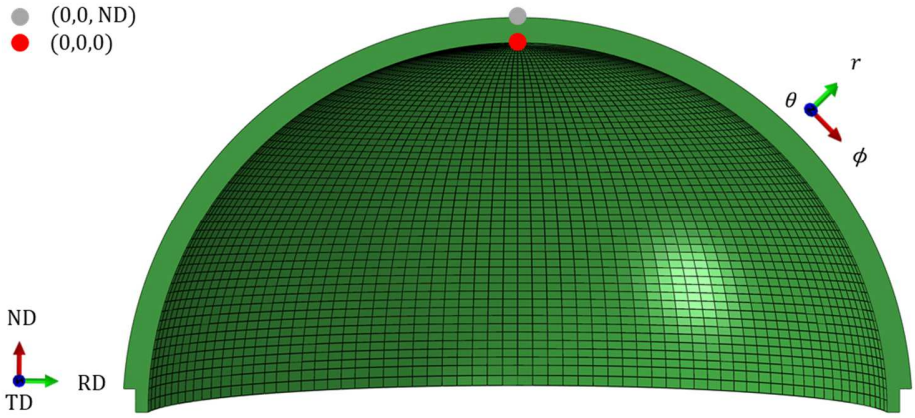

Figure 8. FE mesh of half of the hemi. The half is shown to reveal the displacement boundary conditions at the pole cap, where the two nodes are indicated. Displacement degrees of freedom are fixed in all three global directions for (node red) and in the global rolling direction (RD) and transverse direction (TD) for the (node gray). The global frame and the local frame, θ-azimuthal direction, ϕ-polar direction, and r -radial direction, are shown.

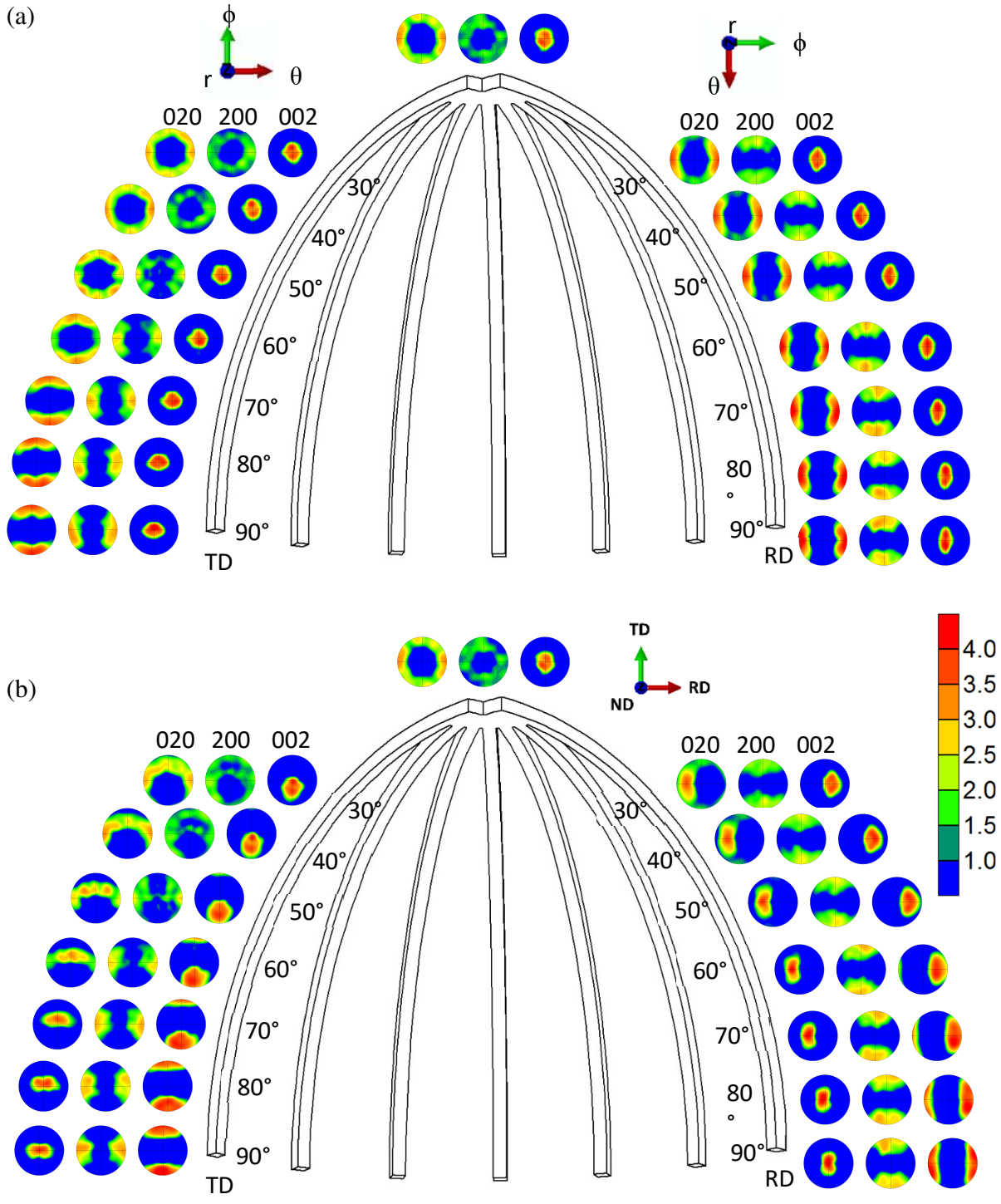

Figure 9. Representation of the arcs cut from the hemi with the polar (ϕ) angles (along arcs) and azimuth (θ) angles (along equator of hemi). Measured pole figures are shown for a few polar angles along the rolling direction (RD) (θ = 0°) and the transverse direction (TD) (θ = 90°). The indicated frames are only for pole figures: a) In the local frame of reference, the pole figure axes

are parallel to the local azimuthal, polar, and radial directions and b) In the global reference frame, the pole figure axis are parallel to the global RD, TD, and normal direction (ND) of the prior rolled plate that was formed into the hemisphere.

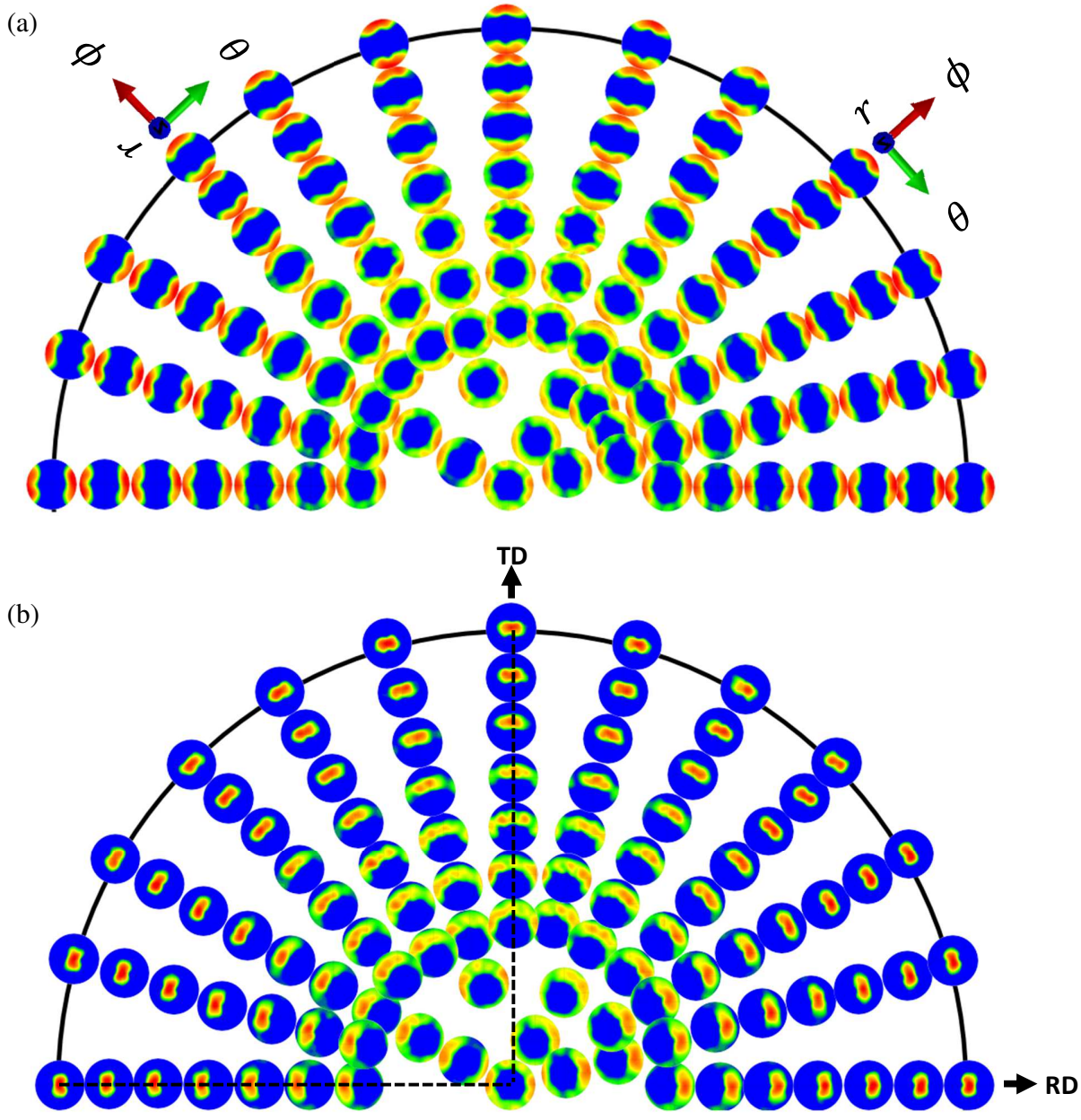

Figure 10. Projected {020} poles on a hemi made of depleted α-U plotted in (a) local moving frame defined by azimuthal direction (θ), polar direction (ϕ), and radial direction (r) and (b) global sample frame defined by RD, TD, and ND. The dashed lines in (b) pass through pole figures shown in Fig. 9. The intensity scale is the same as in figure 9.

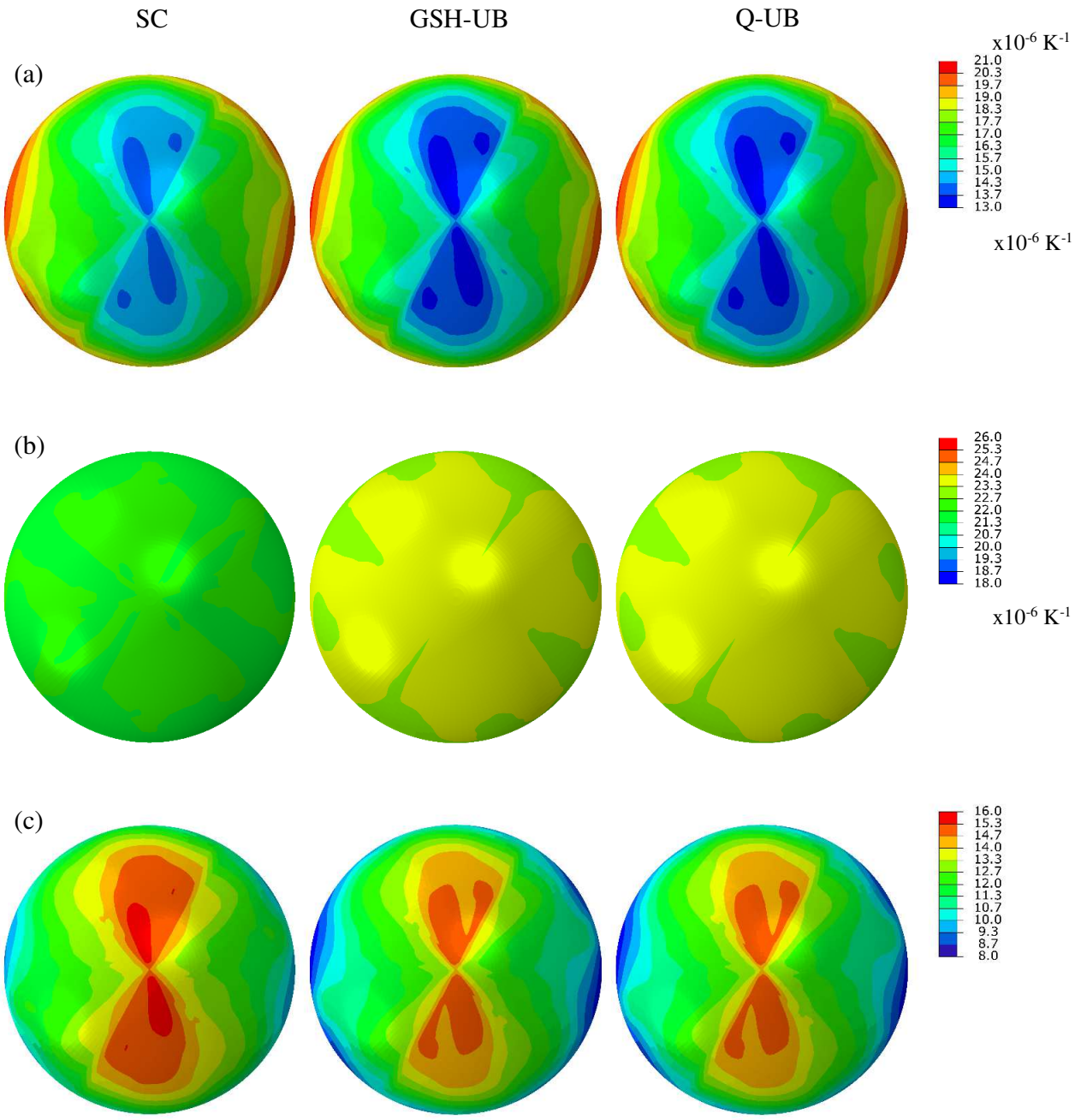

Figure 11. Effective thermal expansion coefficients expressed in the local frame (a) $\bar{\alpha}_{\theta\theta}$, (b) $\bar{\alpha}_{rr}$, and (c) $\bar{\alpha}_{\phi\phi}$ at room temperature based on ODFs at each integration point of the hemisphere after the interpolation. These projections are in the same coordinate system and orientation as those in Fig. 10a.

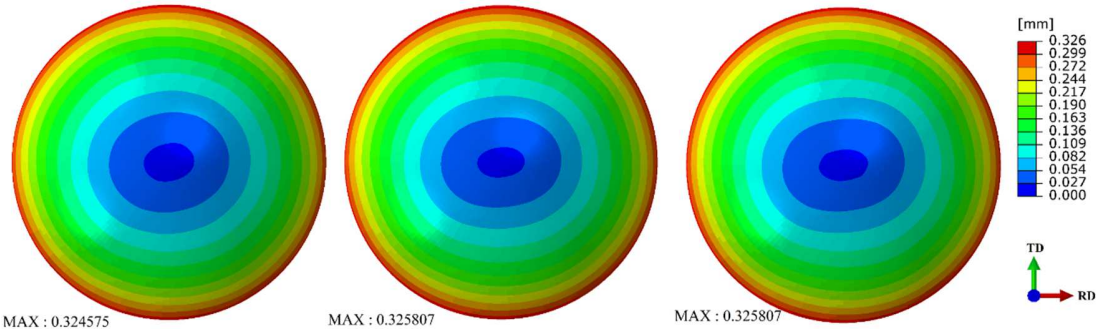

SC GSH-UB Q-UB

Figure 12. Predicted radial displacements (a dot product between displacement vector and radial unit vector) after heating from 25°C to 250°C.

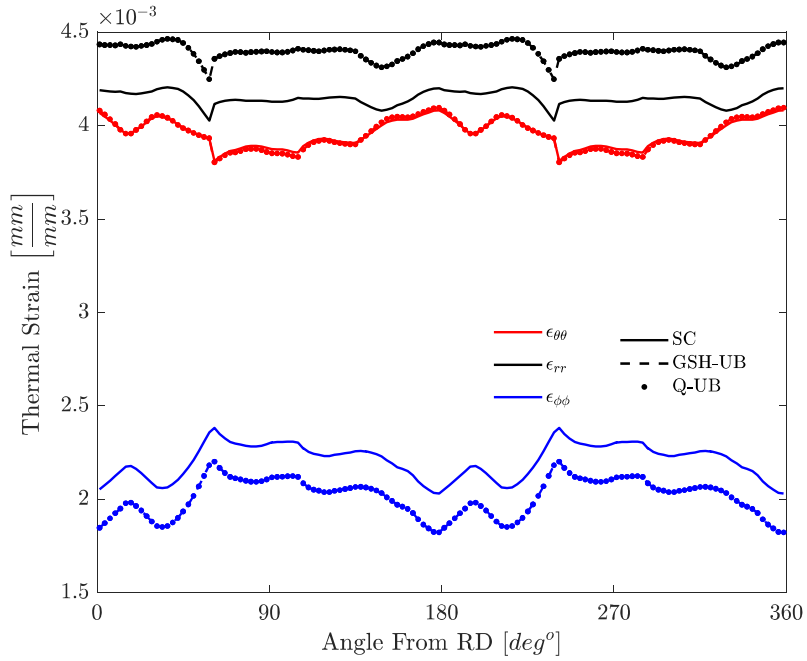

Figure 13. Predicted thermal strains along the hemisphere equator vs orientation from the RD (i.e. the azimuthal angle measured from a global RD coordinate axis) after heating from 25°C to 250°C.

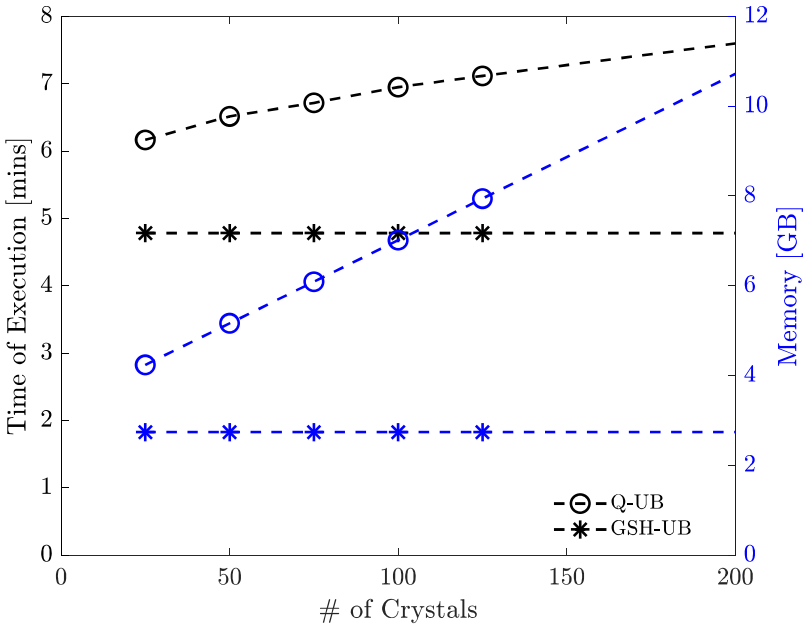

Figure 14. Computational time involved and memory requirements in the heating simulation as a function of the number of orientations embedded at each integration point for two computational methods as defined in the legend.

6. Summary and conclusions

This work developed the computational procedure for microstructure – property linkages for orthorhombic metals using GSH base functions. At the core of the procedure are the databases built to capture the spectral representation of each component of the orientation dependent transformation tensors. The databases are used recursively and efficiently in calculating the bounds of local or homogenized thermal expansion and elastic stiffness/compliance tensors. The procedure is used to delineate the first-order property closures for polycrystalline microstructures of α-U. Numerous examples of thermal expansion and elastic property closures are computed covering a broad range of temperatures. In doing so, certain key properties of these closures are exploited to facilitate their computation with drastically reduced computational effort. The properties of the closures pertain to the invariant texture coefficients corresponding to the boundary points of the closures. The developed computationally efficient ODF-effective property linkages, in conjunction with the recently developed GSH-based interpolation procedure for ODFs from coarsely spaced experimental measurement grids to finely spaced modeling grids, are used to establish a crystal mechanics-based simulation framework coupled with finite elements. The expansion coefficients upon the interpolation are used directly in the GSH-based ODF-property linkages without reconstructing ODFs at every FE integration point. As a result, the thermal expansion and elastic anisotropy are introduced efficiently and elegantly into the numerical FE tool for simulating thermo-mechanical loadings. The GSH approach is

verified by simulating the distortion of a hemispherical part made of α-U during heating by comparing results of the same simulation performed using the upper bound conventional methodology. Additionally, the same results are presented based on the self-consistent homogenization to appreciate the difference between the self-consistent and the upper bound homogenization. The invertible linkages framework can be used to iteratively vary ODFs to design texture in the part for minimized distortion. These aspects, in addition to introducing the plasticity and texture evolution in the framework, will be subject of future research. Additionally, future works will compare predicted displacement and residual stress fields to experimental data for several thermo-mechanically processed parts.

Acknowledgments

This work is based upon a project supported by the National Science Foundation under CAREER grant no. CMMI-1650641.

References

[1] T.J. Barrett, A. Eghtesad, R.J. McCabe, B. Clausen, D.W. Brown, S.C. Vogel, M. Knezevic. A generalized spherical harmonics-based procedure for the interpolation of partial datasets of orientation distributions to enable crystal mechanics-based simulations, Materialia 6 (2019) 100328.
[2] J.H. Panchal, S.R. Kalidindi, D.L. McDowell. Key computational modeling issues in Integrated Computational Materials Engineering, Computer-Aided Design 45 (2013) 4-25.
[3] B.L. Adams, A. Henrie, B. Henrie, M. Lyon, S.R. Kalidindi, H. Garmestani. Microstructure-sensitive design of a compliant beam, J. Mech. Phys. Solids 49 (2001) 1639-1663.
[4] B.L. Adams, S. Kalidindi, D.T. Fullwood. Microstructure-sensitive design for performance optimization, Butterworth-Heinemann, Waltham, MA, USA, 2013.
[5] O.K. Johnson, C.A. Schuh. Texture mediated grain boundary network design in three dimensions, Mechanics of Materials 118 (2018) 94-105.
[6] S.R. Kalidindi, J.R. Houskamp, M. Lyons, B.L. Adams. Microstructure sensitive design of an orthotropic plate subjected to tensile load, International Journal of Plasticity 20 (2004) 1561-1575.
[7] S.R. Kalidindi, J.R. Houskamp. Application of the Spectral Methods of Microstructure Design to Continuous Fiber Reinforced Composites, Journal of Composite Materials 41 (2007) 909-930.
[8] X. Wu, G. Proust, M. Knezevic, S.R. Kalidindi. Elastic-plastic property closures for hexagonal close-packed polycrystalline metals using first-order bounding theories, Acta. Mater. 55 (2007) 2729-2737.
[9] M. Knezevic, N.W. Landry. Procedures for reducing large datasets of crystal orientations using generalized spherical harmonics, Mechanics of Materials 88 (2015) 73-86.
[10] H.-J. Bunge. Texture analysis in materials science. Mathematical Methods, Cuvillier Verlag, Göttingen, 1993.

[11] L. Zuo, M. Humbert, C. Esling. Elastic properties of polycrystals in the Voigt-Reuss-Hill approximation, Journal of Applied Crystallography 25 (1992) 751-755.
[12] P. Van Houtte. Fast calculation of average Taylor factors and Mandel spins for all possible strain modes, Int. J. Plast. 17 (2001) 807-818.
[13] F. Murat, L. Tartar. Optimality conditions and homogenization. In: Non-linear variational problems, A. Marino, L. Modica, S. Spagnolo, M. Deqiovannieds, Pitman, London, 1985.
[14] A.V. Cherkaev. Variational Methods for Structural Optimization, Springer, New York, 2000.
[15] A.V. Cherkaev, L.V. Gibiansky. Extremal structures of multiphase heat conducting composites, International Journal of Solids and Structures 33 (1996) 2609-2623.
[16] K.A. Lurie. A stable spatio-temporal G-closure and Gm-closure of a set of isotropic dielectrics with respect to one-dimensional wave propagation, Wave Motion 40 (2004) 95-110.
[17] G. Proust, S.R. Kalidindi. Procedures for construction of anisotropic elastic–plastic property closures for face-centered cubic polycrystals using first-order bounding relations, J. Mech. Phys. Solids 54 (2006) 1744-1762.
[18] M. Knezevic, S.R. Kalidindi. Fast computation of first-order elastic-plastic closures for polycrystalline cubic-orthorhombic microstructures, Comput. Mater. Sci. 39 (2007) 643-648.
[19] H.K. Duvvuru, M. Knezevic, R.K. Mishra, S.R. Kalidindi. Application of microstructure sensitive design to FCC polycrystals, Materials science forum 546 (2007) 675-680.
[20] M. Knezevic, S.R. Kalidindi, R.K. Mishra. Delineation of first-order closures for plastic properties requiring explicit consideration of strain hardening and crystallographic texture evolution, Int. J. Plast. 24 (2008) 327-342.
[21] L.E. Fuentes-Cobas, A. Muñoz-Romero, M.E. Montero-Cabrera, L. Fuentes-Montero, M.E. Fuentes-Montero. Predicting the Coupling Properties of Axially-Textured Materials, Materials 6 (2013) 4967-4984.
[22] B. Paul. Prediction of elastic constants of multiphase materials, Trans. Metall. Soc. AIME 218 (1960) 36-41.
[23] R. Hill. The elastic behavior of a crystalline aggregate, Proceedings of the Royal Society of London. Series A, Mathematical and Physical Sciences 65 (1952) 349-354.
[24] R. Hill. Elastic properties of reinforced solids: some theoretical principles, Journal of the Mechanics and Physics of Solids 11 (1963) 357-372.
[25] G.I. Taylor. Plastic strain in metals, Journal of the Institute of Metals 62 (1938) 307-324.
[26] G. Sachs. Zur Ableitung einer Fließbedingung. Mitteilungen der deutschen Materialprüfungsanstalten: Sonderheft IX: Arbeiten aus dem Kaiser Wilhelm-Institut für Metallforschung und demStaatlichen Materialprüfungsamt zu Berlin-Dahlem. Springer Berlin Heidelberg, Berlin, Heidelberg, 1929. pp. 94-97.
[27] S.R. Kalidindi, H.K. Duvvuru, M. Knezevic. Spectral calibration of crystal plasticity models, Acta. Mater. 54 (2006) 1795-1804.
[28] J.B. Shaffer, M. Knezevic, S.R. Kalidindi. Building texture evolution networks for deformation processing of polycrystalline fcc metals using spectral approaches: Applications to process design for targeted performance, Int. J. Plast. 26 (2010) 1183-1194.
[29] M. Lyon, B.L. Adams. Gradient-based non-linear microstructure design, J. Mech. Phys. Solids 52 (2004) 2569-2586.
[30] I.Y. Kim, O.L. de Weck. Adaptive weighted-sum method for bi-objective optimization: Pareto front generation, Structural and Multidisciplinary Optimization 29 (2005) 149-158.

[31] T. Fast, M. Knezevic, S.R. Kalidindi. Application of microstructure sensitive design to structural components produced from hexagonal polycrystalline metals, Comput. Mater. Sci. 43 (2008) 374-383.
[32] D.S. Sintay, B.L. Adams. Microstructure design for a rotating disk: with application to turbine engines. IDETC/CIE, 31st Design automation conference. Long Beach, California USA, 2005.
[33] J.R. Houskamp, G. Proust, S.R. Kalidindi. Integration of microstructure-sensitive design with finite element methods: elastic-plastic case studies in FCC polycrystals, International Journal for Multiscale Computational Engineering 5 (2007) 261-272.
[34] G. Saheli, H. Garmestani, B.L. Adams. Microstructure design of a two phase composite using two-point correlation functions, Journal of Computer-Aided Materials Design 11 (2004) 103–115.
[35] S.R. Kalidindi, J.R. Houskamp. Application of the Spectral Methods of Microstructure Design to Continuous Fiber Reinforced Composites, Journal of Composite Materials 41 (2007) 909-930.
[36] S.R. Kalidindi, M. Binci, D. Fullwood, B.L. Adams. Elastic properties closures using second-order homogenization theories: Case studies in composites of two isotropic constituents, Acta. Mater. 54 (2006) 3117-3126.
[37] O. Sigmund, S. Torquato. Design of materials with extreme thermal expansion using a three-phase topology optimization method, J. Mech. Phys. Solids 45 (1997) 1037-1067.
[38] O. Sigmund, S. Torquato. Composites with extremal thermal expansion coefficients, Applied Physics Letters 69 (1996) 3203.
[39] S. Torquato. Modeling of physical properties of composite materials, International Journal of Solids and Structures 37 (2000) 411-422.
[40] B. Xu, F. Arias, S.T. Brittain, X.-M. Zhao, B. Grzybowski, S. Torquato, G.M. Whitesides. Making negative Poisson's ratio microstructures by soft lithography, Advanced Materials 11 (1999) 1186-1189.
[41] H. Bunge. Texture Analysis in Materials Science, Butterworths, London, UK, 1982.
[42] S.R. Kalidindi, M. Knezevic, S. Niezgoda, J. Shaffer. Representation of the orientation distribution function and computation of first-order elastic properties closures using discrete Fourier transforms, Acta. Mater. 57 (2009) 3916-3923.
[43] P. Neumann. Representation of orientations of symmetrical objects by Rodrigues vectors, Textures and Microstructures 14-18 (1991) 53-58.
[44] F.C. Frank. Orientation Mapping, Metallurgical Transactions A 19A (1987) 403-408.
[45] Y. Takahashi, K.i. Miyazawa, M. Mori, Y. Ishida. Quaternion representation of the orientation relationship and its application to grain boundary problems, Trans. Jpn. Inst. Met. 27 (1985) 345-352.
[46] E.S. Fisher. Temperature dependence of the elastic moduli in alpha uranium single crystals, part IV (298 to 923 K), Journal of Nuclear Materials 18 (1966) 39-54.
[47] Y.S. Touloukian, R. Kirby, R. Taylor, P. Desai. Thermophysical Properties of Matter-the TPRC Data Series. Volume 12. Thermal Expansion Metallic Elements and Alloys. New York, NY, USA: THERMOPHYSICAL AND ELECTRONIC PROPERTIES INFORMATION ANALYSIS CENTER LAFAYETTE IN, 1975.
[48] J.F. Nye. Physical properties of crystals: their representation by tensors and matrices, Oxford university press, New York, USA, 1985.

[49] P.R. Morris. Averaging Fourth-Rank Tensors with Weight Functions, J. Appl. Phys. 40 (1969) 447-448.
[50] G. Proust, S.R. Kalidindi. Procedures for construction of anisotropic elasti-plastic property closures for face-centered polycrystals using first order bouding relations, Journal of the Mechanics and Physics of Solids 54 (2006) 1744-1762.
[51] N. Landry, M. Knezevic. Delineation of First-Order Elastic Property Closures for Hexagonal Metals Using Fast Fourier Transforms, Materials 8 (2015) 6326-6345.
[52] B.L. Adams, X. Gao, S.R. Kalidindi. Finite approximations to the second-order properties closure in single phase polycrystals, Acta. Mater. 53 (2005) 3563-3577.
[53] M. Knezevic, R.J. McCabe, R.A. Lebensohn, C.N. Tomé, C. Liu, M.L. Lovato, B. Mihaila. Integration of self-consistent polycrystal plasticity with dislocation density based hardening laws within an implicit finite element framework: Application to low-symmetry metals, J. Mech. Phys. Solids 61 (2013) 2034-2046.
[54] S.R. Kalidindi, C.A. Bronkhorst, L. Anand. Crystallographic texture evolution in bulk deformation processing of FCC metals, J. Mech. Phys. Solids 40 (1992) 537-569.
[55] M. Zecevic, M. Knezevic. Modeling of Sheet Metal Forming Based on Implicit Embedding of the Elasto-Plastic Self-Consistent Formulation in Shell Elements: Application to Cup Drawing of AA6022-T4, JOM 69 (2017) 922-929.
[56] P.A. Turner, C.N. Tomé. A study of residual stresses in Zircaloy-2 with rod texture, Acta Metall. Mater. 42 (1994) 4143-4153.
[57] M. Zecevic, M. Knezevic. A dislocation density based elasto-plastic self-consistent model for the prediction of cyclic deformation: Application to Al6022-T4, Int. J. Plast. 72 (2015) 200-217.
[58] M. Zecevic, I.J. Beyerlein, M. Knezevic. Coupling elasto-plastic self-consistent crystal plasticity and implicit finite elements: Applications to compression, cyclic tension-compression, and bending to large strains, Int. J. Plast. 93 (2017) 187-211.
[59] S.C. Vogel. A review of neutron scattering applications to nuclear materials, ISRN Materials Science 2013 (2013) 1-24.
[60] A. Eghtesad, T.J. Barrett, M. Knezevic. Compact reconstruction of orientation distributions using generalized spherical harmonics to advance large-scale crystal plasticity modeling: Verification using cubic, hexagonal, and orthorhombic polycrystals, Acta. Mater. 155 (2018) 418-432.
[61] R.J. McCabe, L. Capolungo, P.E. Marshall, C.M. Cady, C.N. Tomé. Deformation of wrought uranium: Experiments and modeling, Acta. Mater. 58 (2010) 5447-5459.
[62] T.J. Barrett, R.J. McCabe, D.W. Brown, B. Clausen, S.C. Vogel, M. Knezevic. Predicting deformation behavior of α-uranium during tension, compression, load reversal, rolling, and sheet forming using elasto-plastic, multi-level crystal plasticity coupled with finite elements, J. Mech. Phys. Solids 138 (2020) 103924.